ACS OMEGA

http://pubs.acs.org/journal/acsodf

Article

Structural and Electronic Properties of Single-Atom Transition Metal-Doped Boron Clusters MB_{24} (M = Sc, V, and Mn)

Yue-Ju Yang, Shi-Xiong Li,* De-Liang Chen, and Zheng-Wen Long

Cite This: *ACS Omega* 2021, 6, 30442−30450

Read Online

ACCESS | Metrics & More | Article Recommendations | Supporting Information

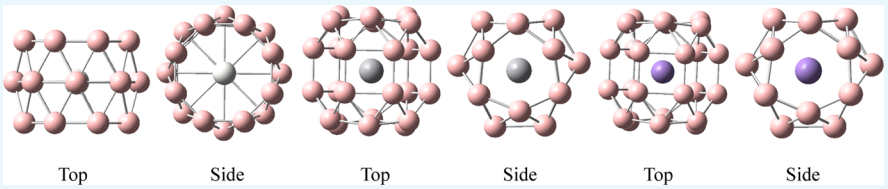

ABSTRACT: A theoretical study of geometrical structures, electronic properties, and spectral properties of single-atom transition metal-doped boron clusters MB_{24} (M = Sc, V, and Mn) is performed using the CALYPSO approach for the global minimum search, followed by density functional theory calculations. The global minima obtained for the VB_{24} and MnB_{24} clusters correspond to cage structures. Interestingly, the global minima obtained for the ScB_{24} cluster tend to a three-ring tubular structure. Population analyses and valence electron density analyses reveal that partial electrons on transition-metal atoms transfer to boron atoms. The localized orbital locator of MB_{24} (M = Sc, V, and Mn) indicates that the electron delocalization of ScB_{24} is stronger than that of VB_{24} and MnB_{24}, and there is no obvious covalent bond between doped metals and B atoms. The spin density and spin population analyses reveal that MB_{24} (M = Sc, V, and Mn) have different spin characteristics which are expected to lead to interesting magnetic properties and potential applications in molecular devices. The calculated spectra indicate that MB_{24} (M = Sc, V, and Mn) has meaningful characteristic peaks that can be compared with future experimental values and provide a theoretical basis for the identification and confirmation of these single-atom transition metal-doped boron clusters. Our work enriches the database of geometrical structures of doped boron clusters and can provide an insight into new doped boron clusters.

1. INTRODUCTION

With the development of science and technology, modern manufacturing technology is moving toward smaller scales. For example, the current semiconductor process has reached the nanometer level. If design and manufacturing can be conducted at the atomic scale, the bottleneck of semiconductor design and manufacturing is expected to be removed and potentially produce disruptive new materials and devices. Clusters are special structures situated between atoms, molecules, and bulk and have different properties compared with bulk materials. For example, the emergence of fullerene C_{60} is a new breakthrough in nanomaterial and nanotechnology,[1] and the discovery of carbon nanotubes and graphene[2,3] promoted carbon nanomaterials to become a vibrant scientific field. The physical properties of clusters are dependent on their size and shape, which can be changed to give them different physical properties owing to the quantum effect of electrons. Theoretical study of the structure and physical properties of clusters can provide guidance for the design and manufacture of new materials and new devices at the atomic level. Boron is a close neighbor of carbon, and scientists have also conducted extensive research on boron clusters. Boron atoms, with only three valence electrons (one less than carbon), can form polycentric chemical bonds and produce several interesting structures and properties.[4−9] Experimental studies have found that anionic pure boron clusters, B_n^-, with less than 38 atoms have a planar or quasi-planar structure.[10,11] Theoretical studies have found that neutral pure boron clusters of different sizes of B_n have planar, tubular, cage-like, or other three-dimensional structures.[4,8,12−14] In 2014, the breakthrough discovery of borospherene[15] B_{40}^- produced a lot of research on boron clusters.[16−24] Similar to fullerenes or carbon nanotubes, boron clusters may be used as molecular devices. Various chemical modifications are carried out to form boron-based nanomaterials with novel structures.

Similar to fullerenes, doping of metal atoms into boron clusters can produce new structures or properties.[18,20−22,25−38] For example, in the case of an alkali metal, experimental research combined with theoretical calculation revealed that B_{20}^-, B_{22}^-, and B_{24} have a quasi-planar structure, quasi-planar structure, and double-ring tubular structure,[10,39] respectively.

Received: July 14, 2021
Accepted: October 21, 2021
Published: November 4, 2021

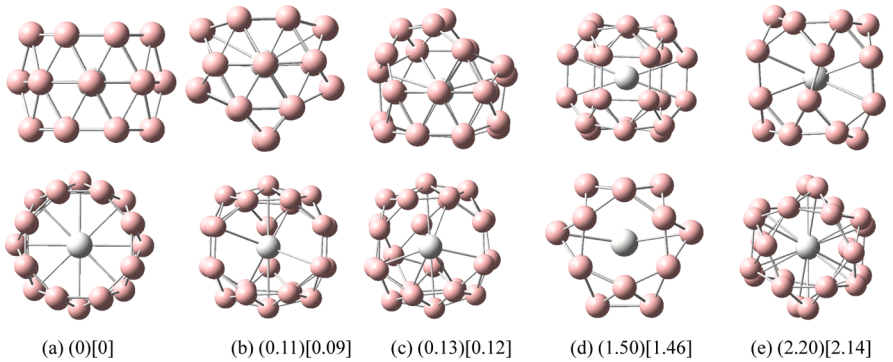

Figure 1. Structures of doped boron clusters ScB_{24}. Values in parentheses are the relative energies (eV) of the five low-energy isomers for ScB_{24} at the PBE0/def2-TZVP level. Values in square brackets are the relative energies (eV) of the five low-energy isomers for ScB_{24} at the PBE0/6-311G* level. The top row is the side view and the bottom row is the top view. (a) I D_{8h}; (b) II C_2; (c) III C_1; (d) IV C_s; and (e) V C_{2h}.

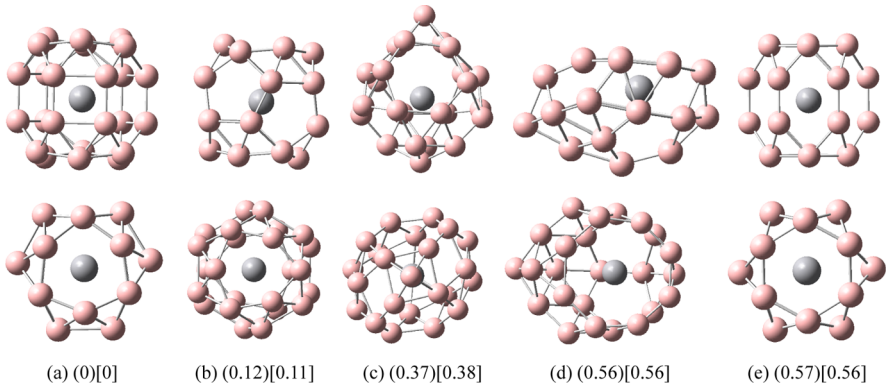

Figure 2. Structures of doped boron clusters VB_{24}. Values in parentheses are the relative energies (eV) of the five low-energy isomers for VB_{24} at the PBE0/def2-TZVP level. Values in square brackets are the relative energies (eV) of the five low-energy isomers for VB_{24} at the PBE0/6-311G* level. The top row is the side view and the bottom row is the top view. (a) I D_3; (b) II C_{2h}; (c) III C_2; (d) IV C_s; and (e) V C_{2h}.

However, both LiB_{20}^- and MB_{22}^- (M = Na and K) possess a double-ring tubular structure and Li_2B_{24} possesses a three-ring tubular structure.[26,40,41] In addition, Li-, Na-, or K-doped borospherene B_{40} is expected to become a nonlinear optical (NLO) nanomaterial.[21] Because of their rich electronic structure characteristics, transition metals can combine with boron clusters to produce rich structures and properties. For example, the quasi-planar B_{12} cluster has a semisandwich structure after being doped with metal atoms such as Co and Rh.[6,25] Neutral B_{24} has a double-ring tubular structure, while TiB_{24} and CrB_{24} have a cage structure after doping with one Ti or Cr atom.[42] The single-atom Sc- or Ti-doped borospherene B_{40} is expected to become a hydrogen-storage material,[18,20,22] transition metal-doped boron clusters MB_{12}^- (M = Co, Rh) can enhance chemical activity,[28] and the single-atom Co-doped B_{40} is expected to be applied in molecular devices.[27] Therefore, the study of transition metal-doped boron clusters provides important theoretical guidance for the study of new structures and new properties of boron clusters and the preparation of new boron nanomaterials. Herein, to obtain the structures and properties of transition metal-doped boron clusters MB_{24} (M = Sc, V, and Mn), extensive research has been conducted on the geometric structure, spectral properties, and electronic structure using the CALYPSO approach,[43] in combination with the density functional theory method PBE0.[44] The calculation results will be useful for future experimental data of MB_{24} (M = Sc, V, and Mn).

2. COMPUTATIONAL METHODS

Geometric structure searches of neutral MB_{24} (M = Sc, V, and Mn) clusters were implemented using particle swarm optimization (CALYPSO) software. CALYPSO is a powerful cluster structure search method, which has been successfully applied to boron and doped boron clusters.[14,26] The PBE0/3-21G level was used for the preliminary structural search. In each generation, 70% of the structures were produced by particle swarm optimization (PSO) operations, while the others were randomly generated. There were nearly 2000 isomers initially obtained for each boron cluster.

Low-energy structures were then fully optimized at the PBE0/def2-TZVP and PBE0/6-311G* levels.[44−46] Different spin multiplicities (doublet, quartet, and sextet) are tested for the system considered during the optimization process. After the geometry optimizations, frequency analyses were conducted and electronic structures were studied at the PBE0/6-311G* level. The PBE0/6-311+G* and PBE0/6-311G* are reliable levels for boron clusters;[15,47−51] specifically, theoretical calculation results with the PBE0/6-311+G* level agree with the experimental results.[15] To test the reliability of the PBE0/6-311G* level, we used the 6-311+G* basis set and 6-311G* basis set to calculate the infrared and Raman spectra, and the results show that the infrared and Raman spectra obtained are found to be almost the same using two basis sets. In addition, the bond length of V−V was simulated with the PBE0/6-311G* level. From the calculated results, the simulated bond length (2.64) of V−V is very close to the experimental bond

https://doi.org/10.1021/acsomega.1c03740
ACS Omega 2021, 6, 30442−30450

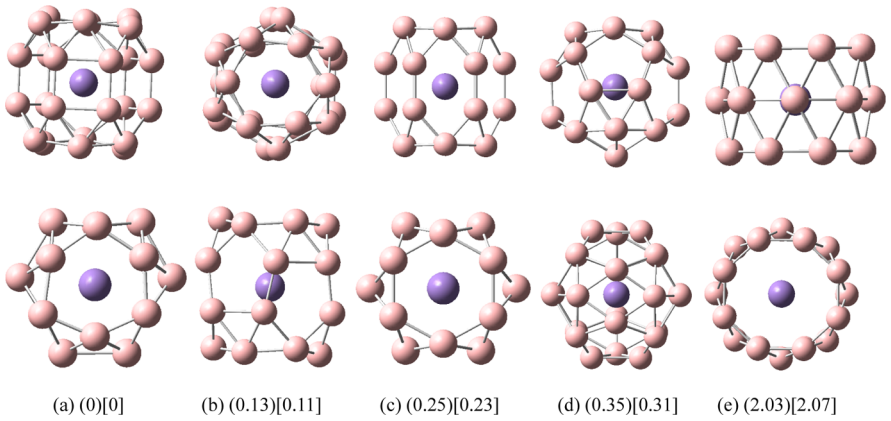

Figure 3. Structures of doped boron clusters MnB_{24}. Values in parentheses are the relative energies (eV) of the five low-energy isomers for MnB_{24} at the PBE0/def2-TZVP level. Values in square brackets are relative energies (eV) of the five low-energy isomers for MnB_{24} at the PBE0/6-311G* level. The top row is the side view and the bottom row is the top view. (a) I C_2; (b) II C_{2h}; (c) III C_{2h}; (d) IV C_1; and (e) V D_{2h}.

Table 1. Lowest Frequencies, Average Binding Energy, Charges on the Doped Atom, Dipole Moments (μ), and Mayer Bond Orders between Doped Metal Atoms and B Atoms of MB_{24} (M = Sc, V, and Mn)

	lowest frequencies/cm^{-1}	average binding energy/eV	charges on doped atom	μ/debye	Mayer bond order between doped atom M and B atom
ScB_{24}	156	5.31	0.50	0	0.14−0.19
VB_{24}	73	5.39	0.80	0	0.17−0.22
MnB_{24}	135	5.31	0.97	0.1	0.08−0.24

length (2.77) of V−V obtained by Langridge-Smith et al.[52] Therefore, the discussion below is on the basis of the PBE0/6-311G* level. All computations were performed using Gaussian 16 software.[53] All analyses and various types of isosurface map drawings were realized using the Multiwfn 3.7(dev) code.[54]

3. RESULTS AND DISCUSSION

3.1. Structures and Electronic Properties. The five low-energy structures of transition metal-doped boron clusters MB_{24} (M = Sc, V, and Mn) are shown in Figures 1−3. The calculation results show that the low-energy structures of MB_{24} (M = Sc, V, and Mn) tend to form cage structures, and the lowest-energy structures of MB_{24} (M = Sc, V, and Mn) are characterized by the lowest spin multiplicity (doublet). Early research found that B_{24} has a double-ring tubular structure, and B_{24}^- has a planar structure. It can be seen from Figure 1 and the calculation results that after adding Sc atoms, the lowest energy structure I of ScB_{24} has a three-ring tubular structure, comprising three eight-membered rings. The lowest energy structure I has high symmetry (D_{8h}), and the Sc atom is located at the center of the tube. The distance between the Sc atom and each B atom on the eight-membered rings at both ends is 2.59 Å, and the distance from the Sc atom to each B atom on the middle eight-membered ring is 2.30 Å. Similar to tubular B clusters, Sc-doped boron clusters are expected to become the basic unit of boron nanotube materials, which will be further synthesized into boron nanotubes.

It can be seen from Figures 2 and 3 that the lowest energy structures of VB_{24} and MnB_{24} have similar cage structures comprising a six-membered ring at each end and two six-membered rings in the middle. Among them, VB_{24} has high symmetry (D_3), and the V atom is located at the center of the cage. The distance between the V atom and each B atom on the six-membered rings at each end of the cage is 2.54 Å, and the distance between the V atom and each B atom on the two six-membered rings in the middle is 2.40 Å. The Mn atom of MnB_{24} slightly deviates from the center of the cage, which leads to a decrease in the symmetry of MnB_{24} (C_2). In the following discussion, the main focus is on the study of the lowest energy structure I.

Some of the ground-state parameters of transition metal-doped boron clusters MB_{24} (M = Sc, V, and Mn) are listed in Table 1, including the lowest harmonic frequency, dipole moment, atomic charge on doped transition-metal atoms, and Mayer bond level.[55] The lowest harmonic frequency analysis (see Table 1 for the lowest harmonic frequencies of each cluster) confirmed that these lowest energy structures are indeed stable (no imaginary frequency). To further illustrate the stability of the clusters, the average binding energy of the clusters is calculated, as follows

$$E_b(MB_n) = [nE(B) + E(M) - E(MB_n)]/(n + 1) \quad (1)$$

The calculation results are listed in Table 1. The average binding energy of MB_{24} (M = Sc, V, and Mn) is approximately 5.3 eV, indicating that the stabilities of MB_{24} (M = Sc, V, and Mn) are not much different.

The charge population analysis shows that all the metal atoms show positive charges, indicating that electrons have been transferred to the boron atoms and the Mn atoms have transferred almost one electron. Because there is more than one outer valence electron of Sc, V, or Mn, only a small part of the electrons has been transferred. Analysis shows that the Mayer bond level of the metal atom M and B atom of these clusters is between 0.08 and 0.24 and it is less than 1, indicating that no obvious covalent bond is formed between the metal atom and the B atom. Because ScB_{24} and VB_{24} have high symmetry, D_{8h} and D_3, their dipole moments are 0. MnB_{24} exhibits a small dipole moment owing to its reduced symmetry, although its structure is similar to that of VB_{24}.

Figures 4 and S1 and S2 (Supporting Information) show the localized orbital locator (LOL)[56] of the valence electrons of ScB_{24}, VB_{24}, and MnB_{24}. The LOL can well-describe the

https://doi.org/10.1021/acsomega.1c03740
ACS Omega 2021, 6, 30442−30450

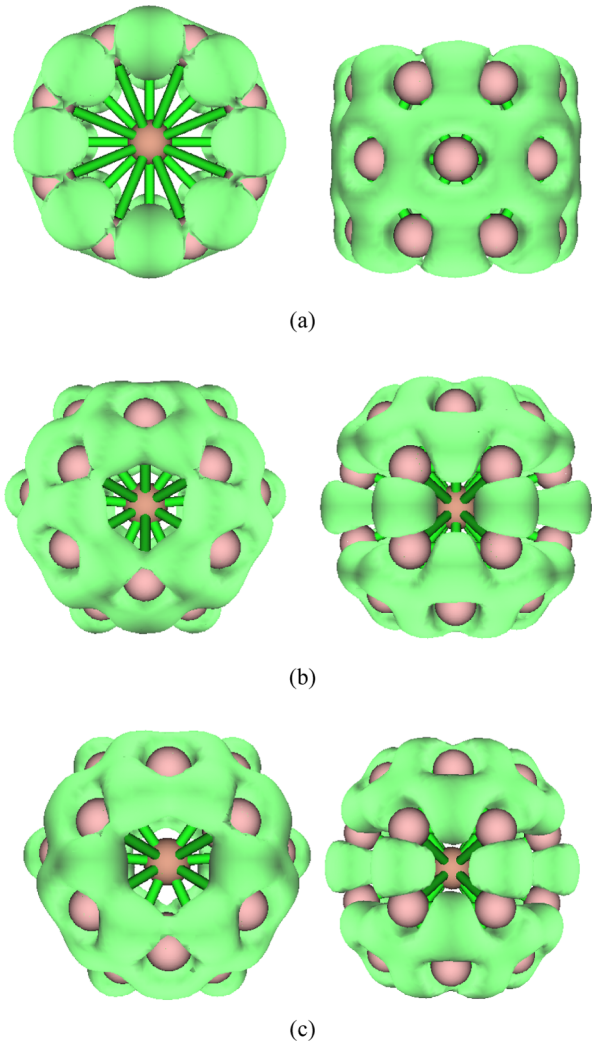

Figure 4. LOL with the isovalue set to 0.62. The left is the top view and the right is the side view. (a) ScB_{24}; (b) VB_{24}; (c) MnB_{24}.

delocalization of electrons. Under the same isosurface value, a fatter (represents the bigger volume and wider connected area occupied by an isosurface map) isosurface means that electron delocalization is easier and a thinner isosurface means that electron delocalization is relatively difficult. When the isosurface value is 0.59 (data not shown), the isosurface maps of ScB_{24} are connected on the tube wall and the isosurface maps of VB_{24} and MnB_{24} are connected on the surface of the cage. Figure 4 shows the LOL when the isosurface value is 0.62. With this isosurface value, the isosurface diagram of ScB_{24} is still connected on the tube wall (both ends of the tube are also connected), while the isosurface diagrams of VB_{24} and MnB_{24} are broken on the surface of the cage. However, the upper and lower halves of the cage are still connected, indicating that the delocalization of the whole ScB_{24} molecule is stronger than that of the other two clusters. Figure 4 also shows that there is a wide blank area around the metal atom, showing that the metal atom does not form an obvious covalent bond with the surrounding B atoms, which is consistent with the Mayer bond level analysis. Figure S1 shows the LOL when the isosurface value is 0.72. Under this isosurface value, the isosurface diagram of ScB_{24} is still connected on the tube wall but the isosurface map is disconnected at both ends of the tube (see the isosurface diagram on the left in Figure S1a). Figure S2 shows the LOL when the isosurface value is 0.73. Under this isosurface value, all the isosurface maps of ScB_{24} are disconnected and there are no connected regions. The isosurface maps of VB_{24} and MnB_{24} show that there is still a connected area in the upper half or lower half of the cage, indicating that the local delocalization of ScB_{24} is weaker than the other two clusters. Tubular-structure ScB_{24} and cage-type VB_{24} and MnB_{24} are expected to become the basic units of boron nanomaterials and be further synthesized into boron nanotubes or other three-dimensional materials. Considering the electron delocalization characteristics of these clusters, they are expected to be applied to molecular devices or molecular switches.

To further characterize the electron localization and chemical bonds, the electron localization function (ELF)[57] of the valence electrons was analyzed, as shown in Figures S3−S5 (Supporting Information). Figures S3−S5 also show that there is a wide blank area around the metal atom, showing that the metal atom does not form an obvious covalent bond with the surrounding B atoms, which is consistent with the Mayer bond level and LOL analysis. In addition, with the increase in the isosurface value, the ELF isosurface shows similar characteristics to the LOL isosurface such as the delocalization of whole ScB_{24} molecule is stronger than that of the other two clusters.

Figures S6 and S7 (Supporting Information) show the isosurface diagrams of valence electron density for ScB_{24}, VB_{24}, and MnB_{24} with isosurface values of 0.16 and 0.20, respectively. Electron density describes the characteristics of electron distribution. Under the same isosurface value, a fatter (represents the bigger volume and wider connected area occupied by an isosurface map) isosurface means more electrons and a thinner isosurface means fewer electrons. The isosurface diagram of Sc is the thinnest and that of Mn is the thickest under the same isosurface value, indicating that the electron density of Mn is the highest. From the previous atomic charge population analysis, we found that the charges on Sc, V, and Mn were 0.5, 0.8, and 0.97, respectively. The valence electrons of Sc, V, and Mn are 3, 5, and 7, respectively, so when the transferred electrons are removed, the remaining valence electrons of Sc, V, and Mn should be 2.5, 4.2, and 6.03. From this, it can be inferred that under the same isosurface value, the isosurface map of the Mn atom is the thickest and that of Sc is the thinnest. In addition, because the B atom has three valence electrons in addition to part of the electrons transferred from the metal atom, it has between 3 and 4 valence electrons. Therefore, the electron density of the B atom should be greater than that of Sc but less than that of V and Mn. The calculation results (isosurface diagrams of valence electron density) show that as the value of the isosurface increases, the isosurface diagram of the Sc atom will disappear first and that of the B atoms in the ScB_{24} will disappear later (as shown in Figures S6a and S7a), indicating that the electron density of the B atoms is greater than that of Sc. With the increase in the isosurface value, the isosurface diagrams of the B atoms in VB_{24} and MnB_{24} will disappear first, and the electron density isosurfaces of V and Mn atoms will disappear later, indicating that the electron density of the B atoms is less than those of the V and Mn atoms. The electron density isosurface diagrams are qualitatively consistent with the atomic charge analysis results.

Figure 5 shows the isosurface diagram of the spin density of ScB_{24}, VB_{24}, and MnB_{24}. Spin density reveals the distribution of unpaired electrons (single electrons) in three-dimensional

https://doi.org/10.1021/acsomega.1c03740
ACS Omega 2021, 6, 30442−30450

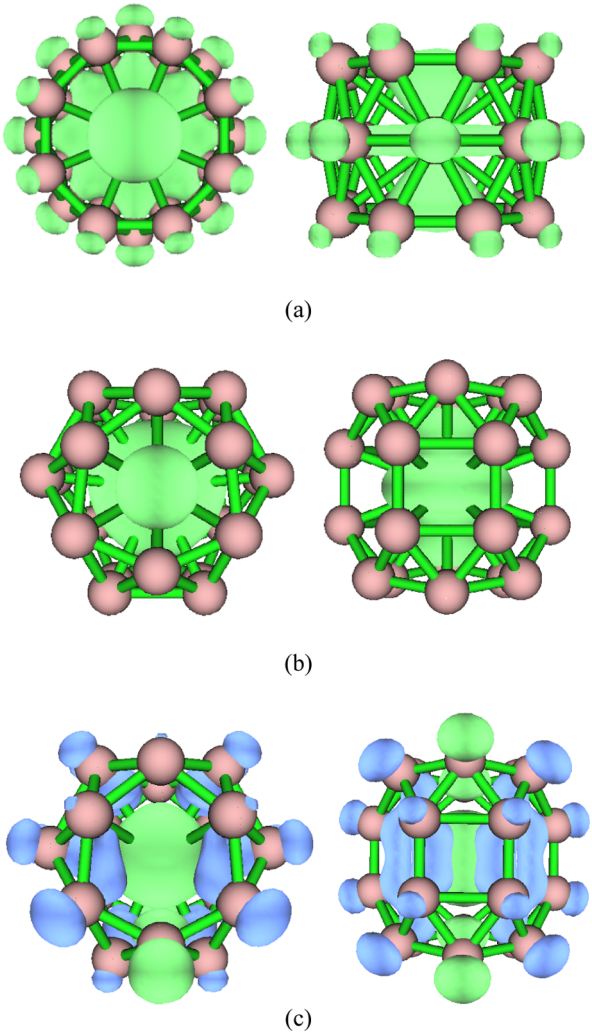

Figure 5. Spin density with the isovalue set to 0.002. Green represents a positive value (α electrons), and blue represents a negative value (β electrons). (a) ScB_{24}; (b) VB_{24}; and (c) MnB_{24}.

space. A positive spin density means that there are more α electrons than β electrons, while a negative spin density means that there are more β electrons than α electrons. Figure 5 shows a spin density diagram for an isosurface value of 0.002. Green represents a positive value (α electrons), while blue represents a negative value (β electrons). It can be seen from Figure 5 that the unpaired single electrons of ScB_{24} are α electrons that are distributed on Sc and B atoms. The unpaired single electrons of VB_{24} are α electrons that are distributed on V atoms. The unpaired single electrons of MnB_{24} are both α and β electrons. Most of the unpaired α electrons are distributed on the Mn atom; only a small part of the unpaired α electrons is on two B atoms. The unpaired β electrons of MnB_{24} are distributed on the other B atoms. To further quantitatively analyze the distribution of unpaired single electrons on different atoms, the spin population is calculated. The spin population is defined as the α electron population minus the β electron population. For example, if the spin population of an atom is one, the α electron population of this atom is one more than its β electron population. A positive population corresponds to an α single electron, while a negative population corresponds to a β single electron. The spin population analysis shows that there is one unpaired α electron in the ScB_{24} system, of which 0.38 is on the Sc atom and the remaining 0.62 is on the B atom. This result is consistent with the spin density diagram. The VB_{24} system has one unpaired single α electron, of which 0.97 is on the V atom and the remaining 0.03 is on the B atom (this basically can be ignored). This result is also consistent with the spin density diagram. Although the total number of unpaired electrons in the MnB_{24} system is 1, 2.01 unpaired α electrons and 1.01 unpaired β electrons are distributed in the system, of which 1.83 α electrons are on the Mn atom and 0.18 α electrons are on the two B atoms; the 1.01 β electrons are distributed on the remaining B atoms. This result is also consistent with the spin density diagram. The spin density reflects chemical reactions or adsorption to a certain extent. The single electrons of ScB_{24} are all α electrons and are basically evenly distributed on the B atoms. The B atoms containing α single electrons can pair with free radicals or small molecules containing β single electrons to form new covalent bonds. For the MnB_{24} system, two B atoms with single α electrons can adsorb or react with free radicals or small molecules with single β electrons, while B atoms with single β electrons can adsorb or react with atoms, free radicals, or small molecules with α single electrons. In addition, these spin features are expected to produce interesting magnetic properties, which will further lead to potential applications in molecular devices.

3.2. Polarization Properties. To understand the polarization properties of the clusters, the polarizability of the system was calculated, including average isotropic polarizability α, average polarizability $\bar{\alpha}$ of a single atom, anisotropic polarizability $\Delta\alpha$, and the first hyperpolarization β_0. α is also called the linear optical coefficient. The anisotropic polarizability describes the response of the system to electric fields from different directions. The larger the value, the stronger is the anisotropic response to the external electric field. The first hyperpolarizability is also called the second-order NLO coefficient, which evaluates the NLO properties of molecules. It can be seen from Table 2 that the polarizability of ScB_{24} is slightly higher than that of VB_{24} and MnB_{24}, indicating that the bonding interactions between the atoms within ScB_{24} are slightly stronger than those of VB_{24} and MnB_{24}, and ScB_{24} is more likely to be polarized by an external electric field. The average polarizability of ScB_{24} is slightly greater than that of VB_{24} and MnB_{24}, indicating that the electronic structures of VB_{24} and MnB_{24} are relatively stable. The anisotropic polarizability of VB_{24} is the smallest and that of ScB_{24} is the largest, indicating that VB_{24} has the weakest anisotropic response and ScB_{24} has the strongest response to an external electric field. It can be seen from Table 2 that the first hyperpolarizability of ScB_{24} is equal to 0, indicating that there is no NLO response; the first hyperpolarizability of VB_{24} is 0.436, indicating that the NLO response is extremely small, and MnB_{24} has a larger first hyperpolarizability, indicating that MnB_{24} has a strong NLO response.

Table 2. Polarizabilities of MB_{24} (M = Sc, V, and Mn)

	α/au	$\bar{\alpha}$ /au	$\Delta\alpha$/au	β_0/au
ScB_{24}	299.047	11.96	27.29	0
VB_{24}	280.658	11.22	12.59	0.436
MnB_{24}	284.329	11.37	19.91	53.83

3.3. Infrared and Raman Spectra. Figures 6 and 7 show plots of the calculated infrared and Raman spectra of MB_{24} (M

https://doi.org/10.1021/acsomega.1c03740
ACS Omega 2021, 6, 30442−30450

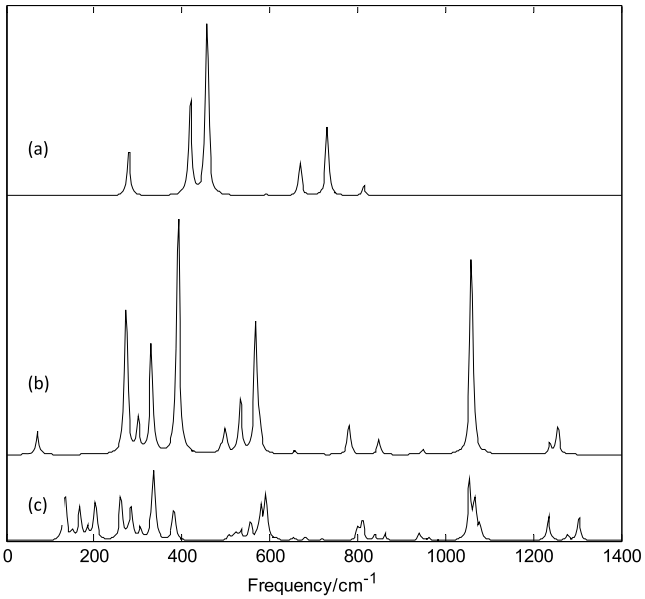

Figure 6. Calculated infrared spectra with the PBE0/6-311G(d) method. (a) ScB_{24}; (b) VB_{24}; and (c) MnB_{24}.

= Sc, V, and Mn) with the PBE0/6-311G(d) method. Figure S8 (Supporting Information) shows the strongest infrared-active vibration mode and Raman-active vibration mode. The lowest harmonic frequencies of these clusters are listed in Table 1. From Table 1 and Figure 6, it can be seen that the cluster structure has a strong influence on the harmonic frequency because these vibration modes are derived from the stretching or bending vibrations of the atoms. Differences in the arrangement of atoms will lead to different modes of vibration. From the calculation results, it can be seen that among the 69 vibration modes of ScB_{24}, only 13 modes are infrared-active and 56 are all inactive. Among the 13 infrared-active modes, five pairs are double-degenerate vibration modes, so there are eight infrared peaks. In the infrared spectrum of ScB_{24}, the first and second peaks are located at 278 and 419 cm^{-1}, respectively, and the second peak is produced by a pair of degenerate vibration modes. The third peak is the strongest, located at 457 cm^{-1}, and is generated by a pair of degenerate vibration modes (in Figure S8a,b). The thick yellow arrow in Figure S8 is the direction vector of the dipole moment changed, caused by the vibration (under resonance approximations, only the infrared intensity of the mode whose dipole moment changes is not zero). The fourth to eighth peaks are located at 592, 669, 731, 813, and 857 cm^{-1}, respectively. The eighth peak is not shown in the figure owing to its weak activity. The fifth, sixth, or eighth peak was generated by a pair of degenerate vibration modes. Among the 69 vibration modes of ScB_{24}, 19 modes are Raman-active vibration modes and 50 are inactive modes. Among the 19 Raman-active modes, eight pairs are degenerate vibration modes. The strongest peak is located at 613 cm^{-1} and is generated by the radial breathing vibration of the boron atoms on the ring (the vibration mode is shown in Figure S8c). This radial breathing mode can reveal important characteristics of nanotubes. It can be seen from the calculation results that the 13 infrared-active modes are Raman-inactive and the 19 Raman-active modes are all infrared-inactive. Under the resonance approximation, the infrared intensity is not zero for only the mode where vibration changes the dipole moment and the Raman activity is not zero for only the mode where vibration changes the polarizability. Therefore, the 13 infrared-active modes did not cause changes in the polarizability and the 19 Raman-active modes did not cause changes in the dipole moment. These vibration characteristics are mainly due to the three-ring structure of ScB_{24} and the high D_{8h} symmetry.

The calculation results show that among the 69 vibration modes of VB_{24}, 41 modes are infrared-active vibration modes and 28 are inactive modes. The strongest infrared peak is also a pair of degenerate vibration modes (the vibration mode is shown in Figure S8d,e). Among the 69 vibration modes of VB_{24}, there are 57 Raman-active modes and 12 inactive modes. The strongest Raman peak is located at 622 cm^{-1}, which is also produced by the radial breathing vibration of boron atoms (the vibration mode is shown in Figure S8f). Among the 69 vibration modes of MnB_{24}, 59 are infrared-active and 10 are inactive. The vibration mode of the strongest infrared peak is shown in Figure S8g. The 69 vibration modes of MnB_{24} are Raman-active modes, and the strongest Raman peak is located at 614 cm^{-1}. This strongest peak is also generated by the radial breathing vibration of boron atoms (the vibration mode is shown in Figure S8h). It can be seen from Figure 6 that VB_{24} and MnB_{24} have some similar band characteristics, but owing to the low symmetry of MnB_{24}, many new band characteristics are also generated, such as several stronger peaks around 200 cm^{-1}. In addition, from Figure 7 and the calculation results, the

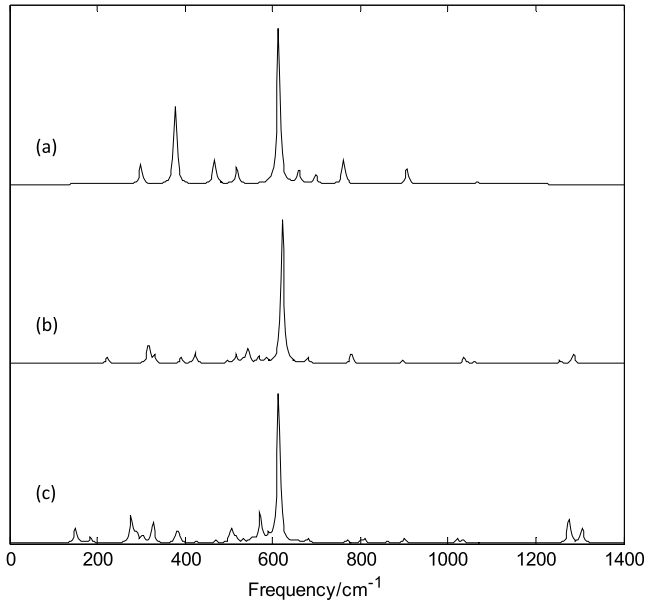

Figure 7. Calculated Raman spectra with the PBE0/6-311G(d) method. (a) ScB_{24}; (b) VB_{24}; and (c) MnB_{24}.

strongest Raman peaks of the three structures are all located at approximately 610 cm^{-1}, and they are all radial breathing modes. Although VB_{24} and MnB_{24} have cage structures, they can be considered variable-diameter tubes. The diameters of the rings are approximately 3.5 Å; therefore, the breathing mode of the three structures is located at approximately 610 cm^{-1}. The characteristic peaks and band characteristics of the clusters can be used to identify these structures, which can be compared and analyzed in future experiments.

3.4. Electronic Absorption Spectra. Based on the previous calculations, the TD-PBE0/6-311G* method was used to calculate the ultraviolet (UV)−visible spectrum of

https://doi.org/10.1021/acsomega.1c03740
ACS Omega 2021, 6, 30442−30450

MB_{24} (M = Sc, V, and Mn) (excitation energy E, wavelength λ, and oscillator intensity f of the first 36 excited states). Figure 8

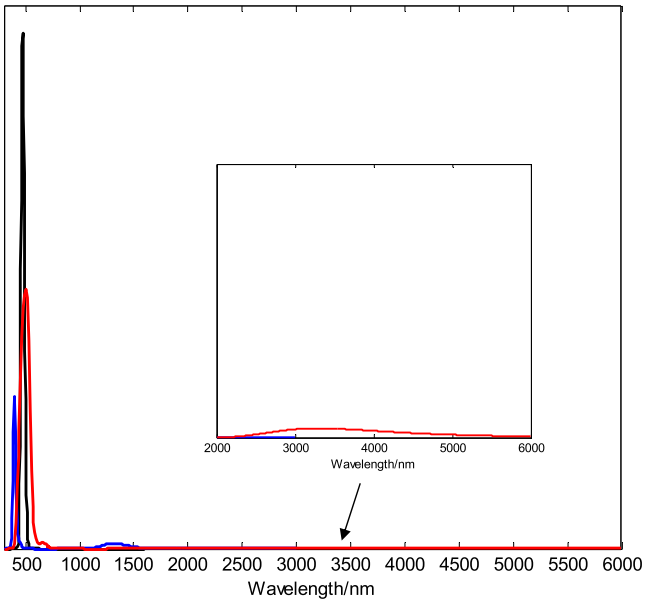

Figure 8. Electronic absorption spectra. The black line represents ScB_{24}, the blue line represents VB_{24}, and the red line represents MnB_{24}.

Table 3. Excitation Properties of MB_{24} (M = Sc, V, and Mn)

	wavelength of the first excited state (oscillator intensity)	first absorption peak (corresponding excited states)
ScB_{24}	1110 nm (0)	474 nm (30)
VB_{24}	1984 nm (0)	1319 nm (3,4)
MnB_{24}	3302 nm (0.0001)	3302 nm (1)

shows the electronic absorption spectra, and Table 3 shows some of the excited-state parameters. It can be seen from Table 3 that except for ScB_{24}, the absorption peaks of these clusters extend to the infrared band. The wavelength of the first excited state of MB_{24} (M = Sc, V, and Mn) is in the infrared band, and the first excited state of ScB_{24} and VB_{24} is the forbidden excited state (oscillator intensity is 0) (see Table 3). The first excited states of ScB_{24}, VB_{24}, and MnB_{24} are mainly derived from the electronic transitions of β-HOMO → β-LUMO, β-HOMO → β-LUMO, and α-HOMO → α-LUMO, respectively. In addition, it can be concluded from Table 3 that the wavelength of the first excited state of MnB_{24} (3302 nm) is the largest, the wavelength of the first excited state of VB_{24} is 1984 nm, and the wavelength of the first excited state of ScB_{24} (1110 nm) is the shortest. Although the structures of VB_{24} and MnB_{24} are similar, their excitation characteristics are obviously different.

From Figure 8 and Table 3, it can be seen that only the first absorption peak of ScB_{24} is in the visible light band and the first absorption peaks of VB_{24} and MnB_{24} are both in the infrared light band. The first absorption peak of MnB_{24} in the main picture of Figure 8 is too weak to be displayed (see the inset for the enlarged absorption peak), which is located at 3302 nm. It can be seen from Table 3 that only the first absorption peak of MnB_{24} corresponds to the wavelength position of the first excited state, and the absorption is very weak. However, because the first and second excited states are forbidden excited states, the first absorption peak of VB_{24} corresponds to the wavelength (1319 nm) of the third and fourth excited states (degenerate). In particular, there is only one absorption peak in the UV−visible spectrum of ScB_{24}, which is derived from the 30th excited state (wavelength is 474 nm), and the other excited states are forbidden excited states. The 30th excited state comes from the electronic transition of α-HOMO → α-LUMO + 7. The electron absorbs the photon to transition from the ground state to the excited state when the vibration intensity is not zero, then transitions from the highly excited state to the low excited state (nonradiative transition), and finally transitions from the lowest excited state back to the ground state and emits light. From the foregoing analysis, it can be inferred that the wavelengths corresponding to the first excited state of these clusters returning to the ground state are all in the infrared light region, so there are emission spectra in the infrared light band. The spectral characteristics of these clusters can be used to identify their structures.

4. CONCLUSIONS

In this work, density functional theory combined with the particle swarm optimization algorithm (CALYPSO) software is used to research the ground-state geometric structure of transition metal-doped boron clusters MB_{24} (M = Sc, V, and Mn). The electronic structures and spectral properties such as infrared and Raman spectra are further discussed. Research results include the following seven points: (1) ScB_{24} has a three-ring tubular structure, while VB_{24} and MnB_{24} have cage structures. (2) Charge population analysis and valence electron density analysis show that doped atoms transfer part of their electrons to boron atoms. (3) The LOL analysis shows that the electron delocalization effect of the entire ScB_{24} molecule is greater than that of VB_{24} and MnB_{24}; however, the metal atoms and the surrounding B atoms do not form an obvious covalent bond. (4) The electron spin density analysis shows that ScB_{24} can adsorb free radicals or small molecules with β single electrons. For the MnB_{24} system, two B atoms with single electrons can adsorb free radicals or small molecules with β single electrons or react with free radicals or small molecules with β single electrons; B atoms with β single electrons can adsorb atoms, free radicals, or small molecules with α single electrons or react with atoms, free radicals, or small molecules with α single electrons. (5) The polarization analysis indicates that the average polarization of each atom of ScB_{24} is greater than that of VB_{24} and MnB_{24}. The first hyperpolarization of ScB_{24} is 0, which indicates that there is no NLO response. (6) The infrared and Raman spectroscopies show that ScB_{24} has eight infrared-active characteristic peaks. The strongest Raman-active modes of ScB_{24}, VB_{24}, and MnB_{24} are located at approximately 610 cm^{-1}. These characteristics can be compared with the experimental values. (7) Through the analysis of the electronic absorption spectra of the clusters, ScB_{24} is found to have the only strong absorption peak in the visible light region, and VB_{24} and MnB_{24} have weaker absorption peaks in the infrared light region. This research has enriched the structure of doped boron clusters and has certain theoretical guiding significance for the preparation of new boron nanomaterials, especially boron nanotubes.

https://doi.org/10.1021/acsomega.1c03740
ACS Omega 2021, 6, 30442−30450

■ ASSOCIATED CONTENT

Supporting Information

The Supporting Information is available free of charge at https://pubs.acs.org/doi/10.1021/acsomega.1c03740.

LOL of MB_{24} (M = Sc, V, and Mn); ELF of MB_{24} (M = Sc, V, and Mn); valence electron density of MB_{24} (M = Sc, V, and Mn); and vibrational modes of MB_{24} (M = Sc, V, and Mn) (PDF)

■ AUTHOR INFORMATION

Corresponding Author

Shi-Xiong Li − *School of Physics and Electronic Science, Guizhou Education University, Guiyang 550018, China;* orcid.org/0000-0003-2831-5955; Email: leesxoptics@163.com

Authors

Yue-Ju Yang − *School of Physics and Electronic Science, Guizhou Education University, Guiyang 550018, China*

De-Liang Chen − *School of Physics and Electronic Science, Guizhou Education University, Guiyang 550018, China*

Zheng-Wen Long − *College of Physics, Guizhou University, Guiyang 550025, China*

Complete contact information is available at: https://pubs.acs.org/10.1021/acsomega.1c03740

Notes

The authors declare no competing financial interest.

■ ACKNOWLEDGMENTS

This work was supported by the National Natural Science Foundation of China (11804065) and the Central Guiding Local Science and Technology Development Foundation of China (grant no. QK ZYD[2019]4012).

■ REFERENCES

(1) Kroto, H. W.; Heath, J. R.; O'Brien, S. C.; Curl, R. F.; Smalley, R. E. C60: Buckminsterfullerene. *Nature* **1985**, *318*, 162−163.

(2) Iijima, S. Helical microtubules of graphitic carbon. *Nature* **1991**, *354*, 56−58.

(3) Novoselov, K. S.; Geim, A. K.; Morozov, S. V.; Jiang, D.; Zhang, Y.; Dubonos, S. V.; Grigorieva, I. V.; Firsov, A. A. Electric field effect in atomically thin carbon films. *Science* **2004**, *306*, 666−669.

(4) Boustani, I. Systematic ab initio investigation of bare boron clusters:mDetermination of the geometryand electronic structures of B_n(n=2−14). *Phys. Rev. B: Condens. Matter Mater. Phys.* **1997**, *55*, 16426−16438.

(5) Zhai, H.-J.; Wang, L.-S.; Alexandrova, A. N.; Boldyrev, A. I. Electronic structure and chemical bonding of B_5^- and B_5 by photoelectron spectroscopy andab initiocalculations. *J. Chem. Phys.* **2002**, *117*, 7917−7924.

(6) Zhai, H.-J.; Kiran, B.; Li, J.; Wang, L.-S. Hydrocarbon analogues of boron clusters–planarity, aromaticity and antiaromaticity. *Nat. Mater.* **2003**, *2*, 827−833.

(7) Kiran, B.; Bulusu, S.; Zhai, H.-J.; Yoo, S.; Zeng, X. C.; Wang, L.-S. Planar-to-tubular structural transition in boron clusters: B_{20} as the embryo of single-walled boron nanotubes. *Proc. Natl. Acad. Sci. U.S.A.* **2005**, *102*, 961−964.

(8) Bean, D. E.; Fowler, P. W. Double Aromaticity in "Boron Toroids". *J. Phys. Chem. C* **2009**, *113*, 15569−15575.

(9) Chen, Q.; Wei, G.-F.; Tian, W.-J.; Bai, H.; Liu, Z.-P.; Zhai, H.-J.; Li, S.-D. Quasi-planar aromatic B_{36} and B_{36}^- clusters: all-boron analogues of coronene. *Phys. Chem. Chem. Phys.* **2014**, *16*, 18282−18287.

(10) Sergeeva, A. P.; Popov, I. A.; Piazza, Z. A.; Li, W.-L.; Romanescu, C.; Wang, L.-S.; Boldyrev, A. I. Understanding boron through size-selected clusters: structure, chemical bonding, and fluxionality. *Acc. Chem. Res.* **2014**, *47*, 1349−1358.

(11) Jian, T.; Chen, X.; Li, S.-D.; Boldyrev, A. I.; Li, J.; Wang, L.-S. Probing the structures and bonding of size-selected boron and doped-boron clusters. *Chem. Soc. Rev.* **2019**, *48*, 3550−3591.

(12) Casillas, R.; Baruah, T.; Zope, R. R. Geometry and electronic structure of neutral and charged B21 clusters. *Chem. Phys. Lett.* **2013**, *557*, 15−18.

(13) Pham, H. T.; Duong, L. V.; Pham, B. Q.; Nguyen, M. T. The 2D-to-3D geometry hopping in small boron clusters: The charge effect. *Chem. Phys. Lett.* **2013**, *577*, 32−37.

(14) Lv, J.; Wang, Y.; Zhu, L.; Ma, Y. B38: an all-boron fullerene analogue. *Nanoscale* **2014**, *6*, 11692−11696.

(15) Zhai, H.-J.; Zhao, Y.-F.; Li, W.-L.; Chen, Q.; Bai, H.; Hu, H.-S.; Piazza, Z. A.; Tian, W.-J.; Lu, H.-G.; Wu, Y.-B.; Mu, Y.-W.; Wei, G.-F.; Liu, Z.-P.; Li, J.; Li, S.-D.; Wang, L.-S. Observation of an all-boron fullerene. *Nat. Chem.* **2014**, *6*, 727−731.

(16) Bai, H.; Chen, Q.; Zhai, H.-J.; Li, S.-D. Endohedral and exohedral metalloborospherenes: M@B_{40} (M=Ca, Sr) and M&B40 (M=Be, Mg). *Angew. Chem., Int. Ed.* **2015**, *54*, 941−945.

(17) Li, S.-X.; Zhang, Z.-P.; Long, Z.-W.; Qin, S.-J. Structures, stabilities and spectral properties of metalloborospherenes $MB_{40}^{0/-}$ (M = Cu, Ag, and Au). *RSC Adv.* **2017**, *7*, 38526−38537.

(18) Dong, H.; Hou, T.; Lee, S.-T.; Li, Y. New Ti-decorated B_{40} fullerene as a promising hydrogen storage material. *Sci. Rep.* **2015**, *5*, 9952.

(19) An, Y.; Zhang, M.; Wu, D.; Fu, Z.; Wang, T.; Xia, C. Electronic transport properties of the first all-boron fullerene B_{40} and its metallofullerene Sr@B40. *Phys. Chem. Chem. Phys.* **2016**, *18*, 12024−12028.

(20) Bai, H.; Bai, B.; Zhang, L.; Huang, W.; Mu, Y.-W.; Zhai, H.-J.; Li, S.-D. Lithium-Decorated Borospherene B_{40}: A Promising Hydrogen Storage Medium. *Sci. Rep.* **2016**, *6*, 35518.

(21) Shakerzadeh, E.; Biglari, Z.; Tahmasebi, E. M@B_{40} (M = Li, Na, K) serving as a potential promising novel NLO nanomaterial. *Chem. Phys. Lett.* **2016**, *654*, 76−80.

(22) Tang, C.; Zhang, X. The hydrogen storage capacity of Sc atoms decorated porous boron fullerene B40: A DFT study. *Int. J. Hydrogen Energy* **2016**, *41*, 16992−16999.

(23) Li, S.; Zhang, Z.; Long, Z.; Chen, D. Structures, Stabilities, and Spectral Properties of Endohedral Borospherenes M@$B_{40}^{0/-}$ (M = H_2, HF, and H_2O). *ACS Omega* **2019**, *4*, 5705−5713.

(24) Li, S.-X.; Zhang, Z.-P.; Long, Z.-W.; Chen, D.-L. Structures, Electronic, and Spectral Properties of Doped Boron Clusters $MB_{12}^{0/-}$ (M = Li, Na, and K). *ACS Omega* **2020**, *5*, 20525−20534.

(25) Popov, I. A.; Li, W.-L.; Piazza, Z. A.; Boldyrev, A. I.; Wang, L.-S. Complexes between planar boron clusters and transition metals: a photoelectron spectroscopy and ab initio study of CoB_{12}^- and RhB_{12}^-. *J. Phys. Chem. A* **2014**, *118*, 8098−8105.

(26) Liang, W.-y.; Das, A.; Dong, X.; Cui, Z.-h. Lithium doped tubular structure in LiB_{20} and LiB_{20}^-: a viable global minimum. *Phys. Chem. Chem. Phys.* **2018**, *20*, 16202−16208.

(27) Wang, W.; Guo, Y.-D.; Yan, X.-H. The spin-dependent transport of transition metal encapsulated B_{40} fullerene. *RSC Adv.* **2016**, *6*, 40155−40161.

(28) Saha, R.; Kar, S.; Pan, S.; Martínez-Guajardo, G.; Merino, G.; Chattaraj, P. K. A Spinning Umbrella: Carbon Monoxide and Dinitrogen Bound MB_{12}^- Clusters (M = Co, Rh, Ir). *J. Phys. Chem. A* **2017**, *121*, 2971−2979.

(29) Li, S.-X.; Chen, D.-L.; Zhang, Z.-P.; Long, Z.-W. Ground state structures and properties of Be atom doped boron clusters BeB_n(n=10−15). *Acta Phys. Sin.* **2020**, *69*, 193101.

(30) Cheung, L. F.; Kocheril, G. S.; Czekner, J.; Wang, L.-S. Observation of Mobius Aromatic Planar Metallaborocycles. *J. Am. Chem. Soc.* **2020**, *142*, 3356−3360.

(31) Popov, I. A.; Jian, T.; Lopez, G. V.; Boldyrev, A. I.; Wang, L.-S. Cobalt-centred boron molecular drums with the highest coordination number in the CoB_{16}^- cluster. *Nat. Commun.* **2015**, *6*, 8654.
(32) Jian, T.; Li, W.-L.; Popov, I. A.; Lopez, G. V.; Chen, X.; Boldyrev, A. I.; Li, J.; Wang, L.-S. Manganese-centered tubular boron cluster - MnB_{16}^-: A new class of transition-metal molecules. *J. Chem. Phys.* **2016**, *144*, 154310.
(33) Chen, T.-T.; Li, W.-L.; Bai, H.; Chen, W.-J.; Dong, X.-R.; Li, J.; Wang, L.-S. ReB_8^- and ReB_9^-: New Members of the Transition-Metal-Centered Borometallic Molecular Wheel Family. *J. Phys. Chem. A* **2019**, *123*, 5317−5324.
(34) Cheung, L. F.; Czekner, J.; Kocheril, G. S.; Wang, L.-S. ReB_6^-: A Metallaboron Analog of Metallabenzenes. *J. Am. Chem. Soc.* **2019**, *141*, 17854−17860.
(35) Chen, T.-T.; Li, W.-L.; Chen, W.-J.; Yu, X.-H.; Dong, X.-R.; Li, J.; Wang, L.-S. Spherical trihedral metallo-borospherenes. *Nat. Commun.* **2020**, *11*, 2766.
(36) Cheung, L. F.; Kocheril, G. S.; Czekner, J.; Wang, L.-S. MnB_6^-: An Open-Shell Metallaboron Analog of 3d Metallabenzenes. *J. Phys. Chem. A* **2020**, *124*, 2820−2825.
(37) Chen, W.-J.; Kulichenko, M.; Choi, H. W.; Cavanagh, J.; Yuan, D.-F.; Boldyrev, A. I.; Wang, L.-S. Photoelectron Spectroscopy of Size-Selected Bismuth-Boron Clusters: BiB_n^- (n = 6-8). *J. Phys. Chem. A* **2021**, *125*, 6751−6760.
(38) Jiang, Z.-Y.; Chen, T.-T.; Chen, W.-J.; Li, W.-L.; Li, J.; Wang, L.-S. Expanded Inverse-Sandwich Complexes of Lanthanum Borides: $La_2B_{10}^-$ and $La_2B_{11}^-$. *J. Phys. Chem. A* **2021**, *125*, 2622−2630.
(39) Chacko, S.; Kanhere, D. G.; Boustani, I. Ab initio density functional investigation of B_{24} clusters: Rings, tubes, planes, and cages. *Phys. Rev. B: Condens. Matter Mater. Phys.* **2003**, *68*, 035414.
(40) Liang, W.-y.; Das, A.; Dong, X.; Wang, M.-h.; Cui, Z.-h. Structural and electronic properties of MB_{22}^- (M = Na, K) clusters: tubular boron versus quasi-planar boron forms. *New J. Chem.* **2019**, *43*, 6507−6512.
(41) Dong, X.; Jalife, S.; Vásquez-Espinal, A.; Barroso, J.; Orozco-Ic, M.; Ravell, E.; Cabellos, J. L.; Liang, W.-y.; Cui, Z.-h.; Merino, G. Li_2B_{24}: the simplest combination for a three-ring boron tube. *Nanoscale* **2019**, *11*, 2143−2147.
(42) Lv, J.; Wang, Y.; Zhang, L.; Lin, H.; Zhao, J.; Ma, Y. Stabilization of fullerene-like boron cages by transition metal encapsulation. *Nanoscale* **2015**, *7*, 10482−10489.
(43) Lv, J.; Wang, Y.; Zhu, L.; Ma, Y. Particle-swarm structure prediction on clusters. *J. Chem. Phys.* **2012**, *137*, 084104.
(44) Adamo, C.; Barone, V. Toward reliable density functional methods without adjustable parameters: The PBE0 model. *J. Chem. Phys.* **1999**, *110*, 6158−6170.
(45) Weigend, F.; Ahlrichs, R. Balanced basis sets of split valence, triple zeta valence and quadruple zeta valence quality for H to Rn: Design and assessment of accuracy. *Phys. Chem. Chem. Phys.* **2005**, *7*, 3297−3305.
(46) Krishnan, R.; Binkley, J. S.; Seeger, R.; Pople, J. A. Self-consistent molecular orbital methods. XX. A basis set for correlated wave functions. *J. Chem. Phys.* **1980**, *72*, 650−654.
(47) Chen, B. L.; Sun, W. G.; Kuang, X. Y.; Lu, C.; Xia, X. X.; Shi, H. X.; Maroulis, G. Structural Stability and Evolution of Medium-Sized Tantalum-Doped Boron Clusters: A Half-Sandwich-Structured TaB_{12}^-Cluster. *Inorg. Chem.* **2018**, *57*, 343−350.
(48) Li, P.; Du, X.; Wang, J. J.; Lu, C.; Chen, H. Probing the Structural Evolution and Stabilities of Medium-Sized $MoB_n^{0/-}$ Clusters. *J. Phys. Chem. C* **2018**, *122*, 20000−20005.
(49) Jin, S.; Chen, B.; Kuang, X.; Lu, C.; Sun, W.; Xia, X.; Gutsev, G. L. Structural and Electronic Properties of Medium-Sized Aluminum-Doped Boron Clusters AlBn and Their Anions. *J. Phys. Chem. C* **2019**, *123*, 6276−6283.
(50) Ren, M.; Jin, S.; Wei, D.; Jin, Y.; Tian, Y.; Lu, C.; Gutsev, G. L. NbB_{12}^-: a new member of half-sandwich type doped boron clusters with high stability. *Phys. Chem. Chem. Phys.* **2019**, *21*, 21746−21752.
(51) Tian, Y.; Wei, D.; Jin, Y.; Barroso, J.; Lu, C.; Merino, G. Exhaustive exploration of MgB_n (n = 10-20) clusters and their anions. *Phys. Chem. Chem. Phys.* **2019**, *21*, 6935−6941.
(52) Langridge-Smith, P. R. R.; Morse, M. D.; Hansen, G. P.; Smalley, R. E.; Merer, A. J. *J. Chem. Phys.* **1984**, *80*, 593−600.
(53) Frisch, M. J.; Trucks, G. W.; Schlegel, H. B.; et al. *Gaussian 16*; Gaussian Inc.: Wallingford CT, 2016.
(54) Lu, T.; Chen, F. Multiwfn: A multifunctional wavefunction analyzer. *J. Comput. Chem.* **2012**, *33*, 580−592.
(55) Mayer, I. Charge, bond order and valence in the ab initio scf theory. *Chem. Phys. Lett.* **1983**, *97*, 270−274.
(56) Schmider, H. L.; Becke, A. D. Chemical content of the kinetic energy density. *J. Mol. Struct.: THEOCHEM* **2000**, *527*, 51−61.
(57) Becke, A. D.; Edgecombe, K. E. A simple measure of electron localization in atomic and molecular systems. *J. Chem. Phys.* **1990**, *92*, 5397−5403.

https://doi.org/10.1021/acsomega.1c03740
ACS Omega 2021, 6, 30442−30450